UC Irvine
UC Irvine Previously Published Works

Title

Unexpected formation of oxygen-free products and nitrous acid from the ozonolysis of the neonicotinoid nitenpyram.

Permalink

Journal

Authors

Wang, Weihong
Ezell, Michael
Lakey, Pascale
et al.

Publication Date

DOI

Unexpected formation of oxygen-free products and nitrous acid from the ozonolysis of the neonicotinoid nitenpyram

Weihong Wang[a], Michael J. Ezell[a], Pascale S. J. Lakey[a] , Kifle Z. Aregahegn[b] , Manabu Shiraiwa[a,1] , and Barbara J. Finlayson-Pitts[a,1]

[a]Department of Chemistry, University of California, Irvine, CA 92697-2025; and [b]Department of Chemistry, Debre Berhan University, Debre Berhan, Ethiopia

The neonicotinoid nitenpyram (NPM) is a multifunctional nitroenamine [$(R_1N)(R_2N)C=CHNO_2$] pesticide. As a nitroalkene, it is structurally similar to other emerging contaminants such as the pharmaceuticals ranitidine and nizatidine. Because ozone is a common atmospheric oxidant, such compounds may be oxidized on contact with air to form new products that have different toxicity compared to the parent compounds. Here we show that oxidation of thin solid films of NPM by gas-phase ozone produces unexpected products, the majority of which do not contain oxygen, despite the highly oxidizing reactant. A further surprising finding is the formation of gas-phase nitrous acid (HONO), a species known to be a major photolytic source of the highly reactive hydroxyl radical in air. The results of application of a kinetic multilayer model show that reaction was not restricted to the surface layers but, at sufficiently high ozone concentrations, occurred throughout the film. The rate constant derived for the O_3–NPM reaction is 1×10^{-18} $cm^3 \cdot s^{-1}$, and the diffusion coefficient of ozone in the thin film is 9×10^{-10} $cm^2 \cdot s^{-1}$. These findings highlight the unique chemistry of multifunctional nitroenamines and demonstrate that known chemical mechanisms for individual moieties in such compounds cannot be extrapolated from simple alkenes. This is critical for guiding assessments of the environmental fates and impacts of pesticides and pharmaceuticals, and for providing guidance in designing better future alternatives.

neonicotinoid | nitenpyram | ozone

Neonicotinoid pesticides (NNs) have largely supplanted other compounds such as the organophosphates, methylcarbamates, and pyrethroids, due to their lower mammalian toxicity (1, 2). Only a small portion (~2 to 20%) (3) of NNs is taken up by the treated crops, and the remainder becomes widely dispersed throughout the environment in water and on surfaces such as soils, vegetation, and windblown dust (3–9). Their increasing use is associated with a decline in the bee population worldwide as well as impacts on nontarget organisms (9–14). As a result, some of the major NNs such as imidacloprid have been banned by the European Union (15) and Canada (16).

Once exposed in the environment (including indoors), they can be converted into a variety of products via photolysis, hydrolysis, and reaction with oxidants such as the OH radical and O_3. Ozone is ubiquitous in air, with concentrations typically ranging from ~20 parts per billion (ppb) to hundreds of ppb in highly polluted environments (17). For some environmental processes, the products are more toxic than the parent compound. For example, the NN imidacloprid is converted by photolysis partly into its desnitro derivative (18–24), which has higher mammalian toxicity than imidacloprid itself (25). It is clearly critical to understand such reactions in order to assess impacts and to provide guidance for the development of more sustainable compounds.

Structural motifs found in the NNs are common to other emerging contaminants such as munitions (26, 27) and pharmaceuticals. For example, the military energetic compound nitroguanidine is closely related to the NN imidacloprid and its analogs. Over-the-counter pharmaceuticals (28) ranitidine and nizatidine (medications for heartburn and gastric disorders) (28) are nitroenamines that contain structural features common to the NNs nitenpyram (NPM), nithiazine, and cycloxaprid.

NPM is used for flea control on animals (29–31), as well as in agriculture, for example, as a treatment on cotton seeds (32–34):
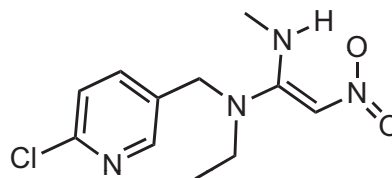
NPM ($C_{11}H_{15}ClN_2O_4$, 270 molar mass).

When present on surfaces such as dust, vegetation, or granules (35), NPM may undergo photolysis and reaction with atmospheric oxidants such as ozone. While the photochemistry of NPM in thin solid films (36) and in aqueous solution (37, 38) has been reported, reactions with ozone have not. There are two potential functional groups for attack, the alkene carbon–carbon double bond and two amine nitrogens. The initial steps in the reaction of O_3 with alkene double bonds are well known (Fig. 1A),

ENVIRONMENTAL SCIENCES

forming an excited primary ozonide (POZ) via addition across the double bond, which then decomposes to form a carbonyl compound and a Criegee intermediate (CI) (39–41). The fate of the CI depends on its environment. In a solid or in an inert solvent cage in solution, it usually recombines with the carbonyl compound to form a stable secondary ozonide (SOZ). Alternatively, the CI can react with other species if available (42), such as water, SO_2, acids, alcohols, peroxy radicals, etc., or decompose to form OH radicals (43, 44). Ozone can also attack amine nitrogens. In the gas phase, this is typically slower than the attack on the C=C bond, although the reaction rate constant with tertiary amines can approach that for alkenes (45). In NPM, the nitrogen p orbitals in the amine groups are conjugated with the π orbitals on the C=C bond and with the $-NO_2$ group on the alkene carbon (36, 46–48), and it is not clear a priori whether unique chemistry will arise due to these interactions.

Results and Discussion

Fig. 2 shows the electrospray ionization mass spectrometry (ESI-MS) (+) of the mixture of solid products and unreacted NPM extracted from the surface of silicon strips after reaction with ozone. Peaks due to the proton, sodium, and potassium adducts of unreacted NPM occur at m/z 271, 293, and 309, respectively, and product peaks are observed at m/z 212, 241, 433 to 441, and 465. Direct analysis in real-time mass spectrometry (DART-MS) studies showed similar peaks (*SI Appendix*, Fig. S1). MS/MS spectra were acquired for each of these peaks (*SI Appendix*, Figs. S2 and S3), and accurate mass measurements were carried out (*SI Appendix*, Table S1). Based on these data, the products shown in Fig. 3 are proposed. The measured accurate mass of each product is consistent with the calculated exact mass, and with the fragmentation patterns for each parent peak. The cluster of peaks at m/z 433 to 441 represents two different products at m/z 433 and 437, with overlapping peaks due to the Cl isotopes (35, 37) (*SI Appendix*, Fig. S4). Note that all of the products tentatively identified by ESI-MS and DART-MS have preserved the tertiary group in NPM, suggesting that attack of ozone on the tertiary amine is not important. This is consistent with studies of the ozonolysis in water of the structurally related pharmaceutical ranitidine where the reaction with the tertiary amine was not important below pH $\approx$ 8 (49).

Solid-phase products were also examined using attenuated total reflectance Fourier transform infrared spectroscopy (ATR-FTIR). Fig. 4 shows the ATR-FTIR spectrum of 20 monolayers (MLs) of solid NPM before exposure to ozone (black line) and the difference spectra after reaction with 1.15 parts per million (ppm)

O_3 for 1 min (blue line, expanded by a factor of 5 for clarity) and for 16 min (red line). Negative bands at 1592 and 1236 cm^{-1} due to the $-NO_2$ moiety represent loss of NPM during the reaction, while positive bands at 1708, 1667, and 1634 cm^{-1} are due to the formation of products. The peaks at 1667 and 1634 cm^{-1} are both assigned to C=N in imines (50). The former represents an isolated C=N group as found in products *A*, *B*, and *D* (Fig. 3). The peak at 1634 cm^{-1} is red-shifted due to conjugation with another group, consistent with product *C*, which is conjugated with a C=C. While product *C* is also an alkene that could, in principle, react further with ozone, its reactivity may be decreased due to smaller electron density in the C=C bond resulting from conjugation with the two imine groups. There may also be a contribution to the 1634-cm^{-1} peak from product *E*, which is conjugated with a C=O group. However, this contribution is expected to be small based on the low ESI-MS relative intensity and the position of the C=O infrared peak at 1708 cm^{-1}, which is red-shifted compared to that expected for an ester (50). A weak carbonyl stretch at 1708 cm^{-1} is evident only at short reaction times. This indicates that the C=O is not increasing with time proportionately with the imine peaks, suggesting it is being removed by secondary reactions at longer reaction times.

It is quite unexpected that, of the five solid phase products observed after ozonolysis, three contain no oxygen, as established by the accurate mass measurements. Previous studies (51–53) of the ozonolysis of enamines in solution reported only oxygen-containing products such as carbonyl–alcohol combinations and hydroperoxides. Furthermore, three of the five products have higher molecular masses than NPM, indicating that reactive intermediates formed in the initial reaction with O_3 must then attack NPM.

The combination of gas- and solid-phase products was interrogated using transmission FTIR in static-mode experiments (*SI Appendix*, Fig. S5A). Fig. 5 shows the difference spectrum when ozone was first added to the cell (black) and that after an hour of reaction (red). Ozone (1054 cm^{-1}) and NPM (1236 cm^{-1}) decreased, and peaks at 791, 852, and 1263 cm^{-1} were observed. These are characteristic of nitrous acid, HONO (54, 55). *SI Appendix*, Fig. S6 shows a typical time dependence for O_3 loss and HONO formation. The HONO concentration crests and then slowly decreases due to slower rates of formation as the ozone is consumed and HONO is lost to the cell walls. Peak HONO concentrations were measured to be in the range $(2.3 \text{ to } 5.0) \times 10^{14}$ molecules$\cdot cm^{-3}$. *SI Appendix*, Table S2 summarizes the HONO yields expressed as the peak HONO formed divided by the corresponding loss of ozone, with an average yield, $\Delta HONO/\Delta O_3$, of 0.12 ± 0.03 (1 σ).
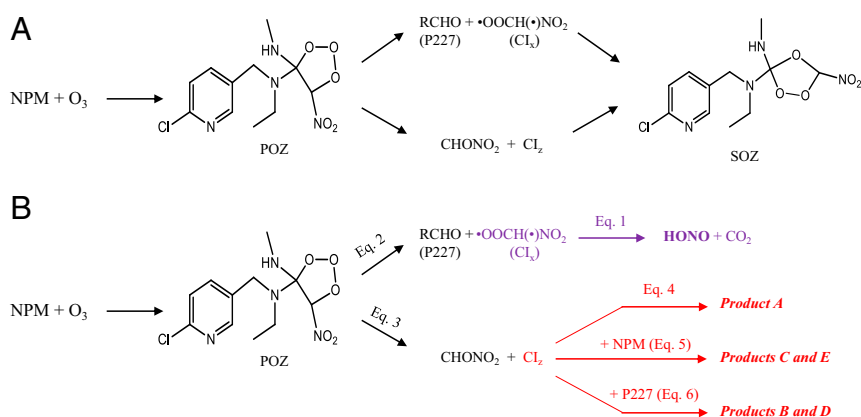
Fig. 1. (*A*) Conventional mechanism of ozonolysis applied to NPM; (*B*) abbreviated proposed mechanism consistent with observed products. Detailed proposed mechanisms for formation of products *A* to *E* are found in *SI Appendix*, Figs. S7–S11.
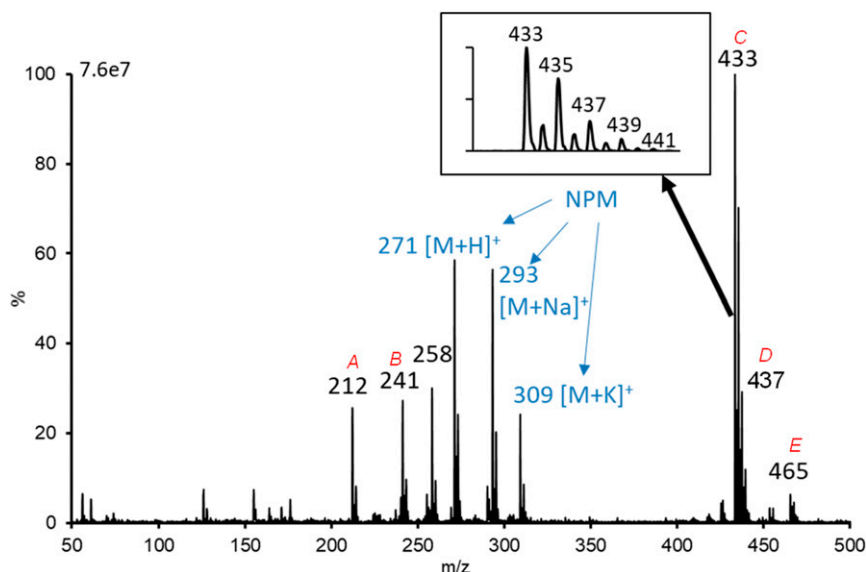
Fig. 2. ESI-MS of the mixture of unreacted NPM and its ozonolysis reaction products labeled *A* to *E* after reaction under a flow of 1.8 ppm O_3 for 1.5 h. *Inset* is an expanded view of the *m/z* 430 to 441 region. The peak at *m/z* 258 does not appear to be a direct reaction product, as it only appeared when water was used as the extraction solvent and was not present in the DART-MS spectrum (*SI Appendix*, Fig. S1).
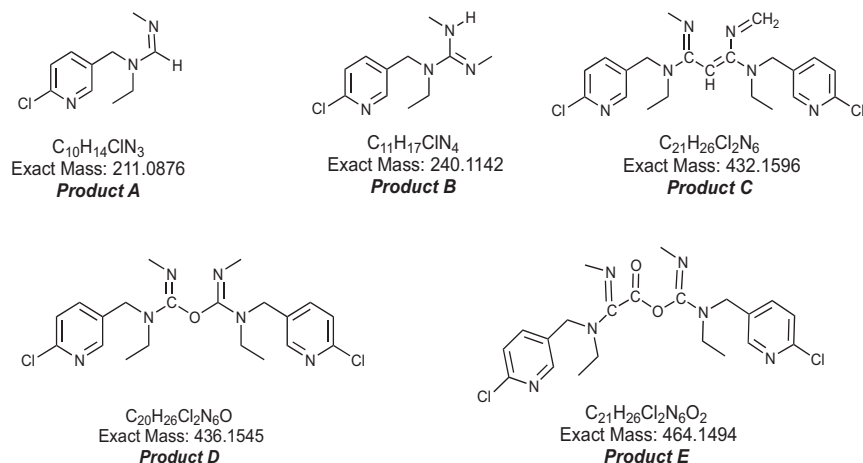
A possible source of HONO in the NPM−ozone reaction is decomposition of the CI that contains the nitro group (CI_x),

$$\bullet OOCH(\bullet)NO_2 \rightarrow HONO + CO_2. \qquad [1]$$

Nitrogen dioxide was never observed in the gas phase, and its heterogenous reaction on surfaces to form HONO is slow (56), ruling this out as a source. To test whether a CI of this type can form HONO, some experiments were also carried out on the reaction of O_3 with gas-phase 2-methyl-1-nitroprop-1-ene, which would be expected to give the same NO_2-CI. Nitrous acid was indeed formed, with an average yield defined as $\Delta HONO/\Delta O_3$ of 0.18 ± 0.05 (1σ), supporting this NO_2−CI as the precursor to HONO (measuring the expected accompanying increase in CO_2 was not possible, due to changes in the background during an experiment). As a further check that the key structural feature in HONO production is an −NO_2 group on the alkene carbon, an experiment was also carried out with 4-methyl-4-nitro-1-pentene where the −NO_2 group is displaced from the alkene double bond, where HONO production was not observed. This provided

further evidence that CI_x was the key intermediate for HONO formation.

As shown in Fig. 1*A*, the ozone reaction with the C=C group in the solid phase should generate a carbonyl group from one side of the double bond and two CIs (CI_x or CI_z) from the other. Recombination to give the SOZ is common in solids. Such a mechanism has been observed, for example, in the ozonolysis on solid substrates of phospholipids (57), as well as alkene self-assembled monolayers (58). While a very small peak around 1105 cm^{-1} was observed in the product FTIR spectrum, similar to that observed in the phospholipid reaction and assigned to the SOZ, there was no ESI-MS peak at *m/z* 318 corresponding to the SOZ in the NPM reaction. Thus, if the SOZ is formed, it must be a minor product. As confirmation, the SOZ from the phospholipid reaction was easily observed by ESI-MS under the same conditions. Conventional ozonolysis mechanisms also predict that formation of the carbonyl product with a molecular weight of 227 (P227) from the larger end of the molecule would accompany the generation of CI_x (the source of HONO). Although a small infrared peak at 1708 cm^{-1} was seen at higher ozone concentrations

$C_{10}H_{14}ClN_3$
Exact Mass: 211.0876
Product A

$C_{11}H_{17}ClN_4$
Exact Mass: 240.1142
Product B

$C_{21}H_{26}Cl_2N_6$
Exact Mass: 432.1596
Product C

$C_{20}H_{26}Cl_2N_6O$
Exact Mass: 436.1545
Product D

$C_{21}H_{26}Cl_2N_6O_2$
Exact Mass: 464.1494
Product E

Fig. 3. Proposed structures and exact masses of solid products from the NPM−O_3 reaction. Note that there are alternate structures of the same exact mass as product *B* that are less likely mechanistically.
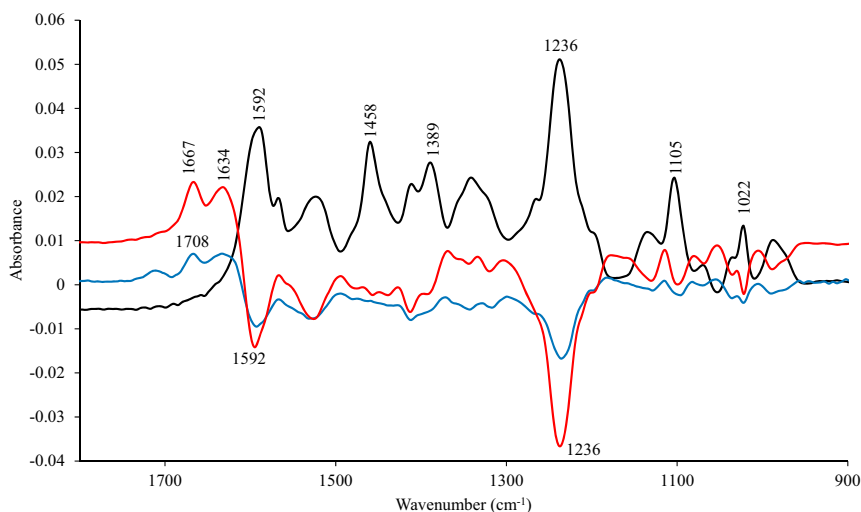
Fig. 4. ATR-FTIR spectrum of 20 MLs NPM before reaction with O_3 (black) and the difference spectra after reaction with 1.15 ppm O_3 for 1 min (blue) or 16 min (red). The blue trace has been expanded by a factor of 5 for clarity of presentation. The ATR spectrum is log (S_0/S_1), where S_0 is the single-beam spectrum of the clean Ge crystal and S_1 is the single-beam spectrum with the thin layer of NPM on the Ge crystal before reaction with ozone. The difference spectrum is log (S_1/S_2), where S_1 is the single-beam spectrum of NPM before reaction and S_2 is the single-beam spectrum after the stated reaction time, so that changes in the spectra compared to the unreacted NPM are more readily seen.

and shorter reaction times, a peak corresponding to P227 was not detected by ESI-MS, suggesting this product is lost to secondary reactions as it is being formed.

Assuming that the first steps in the reaction produce CIs (Fig. 1), that formed from the larger part of the molecule, CI_z, will be generated and can decompose or attack neighboring molecules (NPM or the P227 product). *SI Appendix*, Figs. S7–S11 shows possible mechanisms for formation of products *A* to *E* (Fig. 3). While such mechanisms cannot be proven, they are reasonable and, unlike the conventional ozonolysis mechanisms, can explain the observed products. Note that the proposed mechanism to generate product *B* (mass 240) and product *D* (mass 436) involves secondary chemistry of the carbonyl compound of mass 227, consistent with the 1708-cm^{-1} peak being observable only at the higher ozone concentrations and shorter reaction times. In short, highly unusual chemistry must be taking place in the O_3 reaction with NPM in the solid phase.

The kinetics of the loss of NPM were monitored with ATR-FTIR (*SI Appendix*, Fig. S5B) using the band at 1236 cm^{-1}. *SI Appendix*, Fig. S12 shows typical pseudo−first-order decays for the loss of NPM,

$$\ln\frac{A}{A_0} = -k[O_3]t = -k't,$$

where A is the absorbance at time t and A_0 is the initial absorbance before reaction. The loss of NPM follows first-order kinetics up to a large net loss of NPM. Indeed, at sufficiently long exposures, essentially all of the NPM is reacted. The pseudo−first-order rate constants for decay of ozone, k', were derived for losses up to 50%, and are summarized in *SI Appendix*, Table S3.

A common phenomenon for heterogeneous reactions of solids is surface passivation, where reaction of the top few layers forms a thin layer of unreactive products that shields the underlying
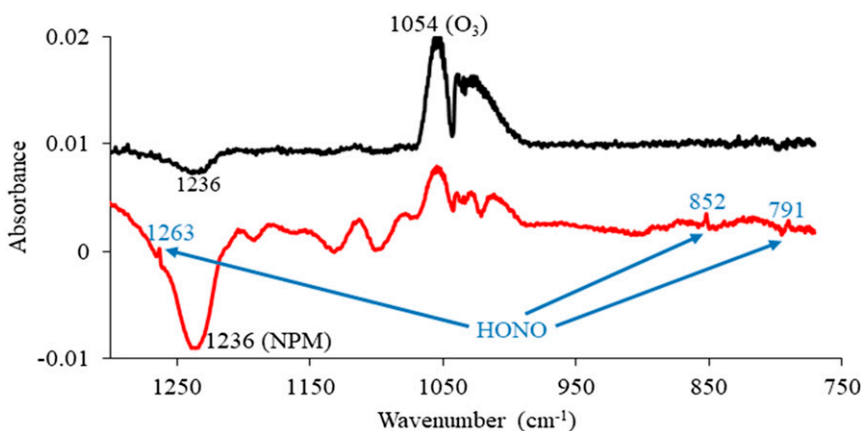
Fig. 5. Transmission spectra of the combined gas and solid phase when thin films of NPM on Si strips were exposed to O_3 in the cell shown in *SI Appendix*, Fig. S5A. As described in *Materials and Methods*, NPM was also deposited on the cell windows in order to detect loss of NPM when O_3 was added. The spectrum shown in black is the difference spectrum when ozone was first added to the cell, log (S_1/S_2), where S_1 is the single-beam spectrum of the cell with thin films of NPM on the windows before addition of O_3 and S_2 is the single-beam immediately after O_3 (6.3 × 10^{15} molecules·cm^{-3}) was added to the cell. The spectrum shown in red is the difference spectrum after an hour of reaction with O_3. The total initial number of NPM was 6.5 × 10^{17} molecules, and that of O_3 was 3.8 × 10^{17} molecules in the 60-cm^3-volume cell.

layers from further reaction (59–61). In this case, the rate of uptake of the reacting gas decreases with time, eventually leading to zero uptake and no further reaction of the solid. However, there was no evidence for surface passivation here, and, at sufficient ozone exposures (combination of time and ozone concentration), almost complete loss of NPM occurs. Thus, diffusion throughout the film along with reaction must take place, which is important for accurately assessing its fate in the environment.

To explore this further, the kinetic multilayer model for aerosol surface and bulk chemistry (KM-SUB) model (62) was applied to quantitatively examine the roles of diffusion and reaction throughout the film, providing key insights into both the experiments and considerations that are important in understanding its reactions with ozone in air. The reaction scheme is summarized in Fig. 1B. While the simplified set of reactions is meant to represent the formation of the observed products without implying mechanisms, it is consistent with those shown in *SI Appendix*, Figs. S7–S11. Eq. 2 (Fig. 1B) represents the first decomposition path for the POZ, generating the CI_x that forms HONO as well as the mass 227 product (P227). Eq. 3 represents the second pathway for the POZ decomposition, giving the larger CI_z which generates product *A* (Eq. 4), and reacts either with NPM (Eq. 5) to generate products *C* and *E* or with P227 that was generated in the first decomposition to form products *B* and *D* (Eq. 6).

SI Appendix, Fig. S13 compares, for the best-fit input parameters summarized in *SI Appendix*, Table S4, the loss of NPM as a function of time predicted by KM-SUB (solid line) to the experimental data (symbols). These represent the best-fit combination of diffusion and reaction kinetics. Good fits to the experimental data are obtained over a broad range of conditions. *SI Appendix*, Fig. S14 shows contour plots of the predicted evolution of NPM and ozone throughout the film as a function of time at a low and a high ozone concentration. Also shown are predicted contours for the products P227, *A*, and the combination of *C* + *E*. At low O_3 concentrations, the reaction occurs near the surface, while, at higher ozone concentrations, reaction occurs throughout the film, highlighting the importance of considering both reaction and diffusion. Note that the predicted peak concentrations of P227 are several orders of magnitude less than the other products, consistent with the difficulty in detecting this product. Another insight from these contours is that reaction is occurring throughout the film at the high O_3 concentrations used in the static HONO measurement experiments. This is consistent with the absolute number of HONO that was generated, which corresponded to reaction of ∼34 to 55 MLs of NPM, assuming an average 12% HONO yield.

The rate constant for the NPM–O_3 reaction derived from the model is 1×10^{-18} $cm^3 \cdot molecule^{-1} \cdot s^{-1}$, and an initial reaction probability is estimated to be ∼9×10^{-6} after taking into account diffusion and depletion of reactant in the surface layer. This is similar in magnitude to that for the gas-phase ozonolysis of disubstituted or trisubstituted simple alkenes (17). The diffusion coefficient for O_3 in NPM, $D = 9 \times 10^{-10}$ $cm^2 \cdot s^{-1}$, is in the range of values expected for diffusion in an amorphous solid (63).

These studies clearly illustrate that reaction products and mechanisms for complex, multifunctional compounds cannot be accurately predicted based on those of the individual structural features. In the case of the neonicotinoid NPM, there is little evidence that the expected SOZ was formed. Instead, highly unusual products that do not contain oxygen are generated, despite the highly oxidizing environment. A thorough literature search showed no mention of oxygen-free products from the ozonolysis of an alkene. In addition, products with much higher molecular masses than the parent compound are generated, indicating cross-reactions of reactive intermediates with NPM or with products formed in the initial NPM–O_3 chemistry. The production of the higher molecular mass products requires that the CI generated

from the larger side of the molecule is formed close to another NPM or its reaction products. Application as granules or being picked up on dust surfaces after application to soils will result in NPM being present as aggregates of various sizes, so this chemistry should apply. In the case of isolated NPM, for example, through systemic uptake in plants, this CI may react with other components of the matrix rather than NPM.

The difference between the ozonolysis mechanism proposed here (Fig. 1B) and the conventional mechanism for alkenes (Fig. 1A) may be due to several factors. First, diffusion of the smaller fragments (CI_x and $CHONO_2$) may be sufficiently fast in the disrupted film that it limits cycloaddition to form the SOZ. Thus, while the diffusion coefficients for CI_x and $CHONO_2$ are expected to be smaller than that for O_3 (9×10^{-10} $cm^2 \cdot s^{-1}$) due to their size, they could still be in the range of 10^{-10} $cm^2 \cdot s^{-1}$ to 10^{-11} $cm^2 \cdot s^{-1}$. If the distance that CI_x and $CHONO_2$ must travel to diffuse away from the larger fragment so they do not recombine is ∼1 nm, then the corresponding diffusion time is on the order of 0.1 ms to 1 ms. Two other processes compete with diffusion: the decomposition of the CI and its 1,3 dipolar cycloaddition to the carbonyl to form SOZ. The decomposition of thermalized CI is typically on the order of ∼10^2 s^{-1} to 10^3 s^{-1}, giving lifetimes of ∼1 ms to 10 ms (42, 44, 64), similar to the diffusion times. The cycloaddition may have steric requirements that are further limited by slower motions in the solid, rendering SOZ formation from the 1,3-cycloaddition less competitive.

Nitrous acid is generated in the gas phase, with indications that it results from the decomposition of the –NO_2 containing CI. This acid absorbs strongly in the actinic region that reaches Earth's surface, and, through its photolysis, it is a major source of the OH radical that drives the chemistry of the atmosphere (17, 65). While the NPM–O_3 reaction is not expected to be a significant source of HONO relative to other known outdoor and indoor sources on a global basis (66, 67), it may play a role locally where NPM is used, and its production in this reaction is certainly of mechanistic interest.

Taken together, these very unusual and surprising results illustrate that accurately assessing the environmental fates of such multifunctional compounds requires detailed, case-by-case studies. Such studies will remain essential at least until much more is known that will permit structure−reactivity relationships to be developed. Understanding such mechanisms and products will provide important guidance in designing the next generation of compounds such as pesticides and pharmaceuticals in order to minimize deleterious impacts.

Materials and Methods

Solid Product Analysis. Product studies were carried out using the cell shown in *SI Appendix*, Fig. S5A. Briefly, solutions of NPM in acetonitrile (ACN) were evaporated onto Si strips (total surface area 15 cm^{-2} to 30 cm^{-2}) which were placed in the cell. Si strips were first cleaned using a plasma cleaner in Ar. The total number of NPM molecules on the strips was in the range of (1.2 to 11) × 10^{17} molecules. Mixtures of ozone in oxygen were generated by photolysis of O_2 (Praxair, 99.993%) using a low-pressure mercury lamp (UV Products, model D-23017). To obtain lower concentrations than could be generated from photolysis, the O_3/O_2 mixture was diluted with N_2 (Praxair, 5.0 grade) in a 5-L glass mixing bulb. The O_3/O_2 (1 part per million [ppm] to 2 ppm) mixture flowed through the cell for a total reaction time of 1 h to 2 h. After exposure to ozone, the mixture of products and unreacted NPM on the Si strips was extracted using 20% ACN and 80% water. The product solution was then further diluted in water for analysis in ESI-MS/MS (Waters, Xevo TQ-S) operated in positive ion mode for full-scan MS and for product ion scans. The solution was injected directly into the ESI-MS source in infusion mode (no chromatography). The parameters for ESI-MS were as follows: cone voltage, 50 V; capillary voltage, 3.2 kV; source temperature, 120 °C; desolvation temperature, 350 °C; desolvation gas (N_2) flow, 1,000 L/h; collision energy for MS/MS, 2 eV to 20 eV; collision gas (Argon) flow, 0.12 mL/min.

The accurate mass of the products was also measured using ion mobility spectrometry (IMS) coupled with quadrupole time-of-flight high resolution mass spectrometry (QTOF-HRMS) (Waters, Synapt G2) and a poly(ethylene

glycol) standard for calibration. The sample solution was introduced into the IMS-QTOF system directly without chromatography. Parameters were as follows: source cone voltage, 37 V; cone gas flow, 50 L/h; capillary voltage, 2.8 kV; source temperature, 85 °C; desolvation temperature, 180 °C; desolvation gas (N_2) flow, 450 L/h; IMS gas control, 50 mL/min; IMS wave velocity, 750 m/s and wave height 24 V; TOF-MS cone voltage, 0 V to 10 V. The accurate mass measurements were confirmed using a ThermoFisher Q Exactive Plus Hybrid Quadrupole-Orbitrap Mass Spectrometer. The sample was infused directly into the heated electrospray ionization source with the following settings: capillary temperature set at 320 °C, S-Lens RF level set at 50, spray voltage set at 6.0 kV, sheath gas flow set at 48, auxiliary gas flow set at 11, and the sweep gas flow rate setting of 2.

In some experiments, a metal screen (stainless steel, 74 mesh 0.094 mm diameter) was used in place of the Si strips for direct analysis with DART (68, 69) (IonSense, DART SVP with Vapur Interface) coupled with a mass spectrometer (Waters, Xevo TQ-S) operated in positive ion mode. The screens with NPM samples before and after reaction with O_3 were moved through the DART ionization region for sample analysis. The parameters used were helium reagent gas flow, 3.1 L/min; source temperature, 400 °C; grid electrode voltage, 350 V.

NPM was used as received (Sigma-Aldrich, 99.5% or Selleckchem, >99%). All experiments were carried out at room temperature, 298 ± 2 K.

Gas-Phase Products. A search for gas-phase products in static-mode experiments using transmission FTIR was carried out using the same cell with Si strips described above (*SI Appendix*, Fig. S5A). In addition to NPM deposited on Si strips, some NPM was also evaporated from solution onto the end windows of the cell in order to directly detect loss of the NPM when ozone was added. Mixtures of O_3 in O_2 (140 ppm to 430 ppm) were added to the cell, and the gas phase was interrogated using FTIR. The cell volume was 60 cm^3, giving a total initial number of O_3 in the cell in the range of (2.1 to 6.3) × 10^{17}. The gas phase was monitored using transmission FTIR (Mattson Cygnus 100, 0.5-cm^{-1} resolution, 128 scans). NPM, deposited on the windows, was also detected. However, using this signal to quantify the NPM loss turned out not to be possible, due to uncertainties in the fraction of the NPM on the windows that was interrogated by the infrared beam.

Gas-Phase Ozonolysis of 2-Methyl-1-nitroprop-1-ene and 4-Methyl-4-nitro-1-pentene. For comparison to the ozone reaction with solid NPM, the gas-phase ozonolysis reactions of 2-methyl-1-nitroprop-1-ene (NTP, AK Scientific, 96%) and 4-methyl-4-nitro-1-pentene (MNP, Musechem, 96%) were also studied using the cell in *SI Appendix*, Fig. S5A in the absence of the Si strips. NTP is a nitromethylene, like NPM, having a terminal =CHNO$_2$ group, while MNP has a nitro group remote from the double bond. Concentrations of NTP (or MNP) ranging from 0.079 × 10^{17} molecules·cm^{-3} to 1.3 × 10^{17} molecules·cm^{-3} (320 ppm to 5,285 ppm) were added, and O_3/O_2 mixtures expanded into the cell to give O_3 concentrations from 0.33 × 10^{16} molecules·cm^{-3} to 1.0 × 10^{16} molecules·cm^{-3} (134 ppm to 407 ppm). Transmission infrared spectra were recorded as a function of time using a Mattson Research Series FTIR at 0.5-cm^{-1} resolution and 32 scans.

Kinetics Studies by ATR-FTIR. Thin films of NPM were deposited by evaporation of a solution in acetonitrile on an attenuated total reflectance (ATR) crystal (Ge, 4 mm × 10 mm × 80 mm, 45°, Pike Technologies) and this was mounted in a holder that was part of a custom-designed cell (*SI Appendix*, Fig. S5B). The available surface area of the crystal was 4 cm^2, and the total amount of NPM deposited on this area varied from 1.3 × 10^{16} molecules to 4.9 × 10^{16} molecules. This was determined by comparison to a calibration of bulk NPM solutions in ACN (25 mM to 74 mM) using the concentration of the solution (number of NPM per cubic centimeter) and the effective thickness probed (d_e) at 1236 cm^{-1}, calculated as 0.42 μm (70). The size of the unit cell of NPM (71) was used to estimate a surface area per molecule (4.75 × 10^{-15} cm^2) and hence the number of molecules per square centimeter in an ML, 2.1 × 10^{14} molecules·cm^{-2}. One ML on the 4-cm^2 crystal therefore corresponds to 8.4 × 10^{14} molecules, so that the amounts on the crystal corresponded to 16 MLs to 59 MLs. The maximum thickness of the film corresponds to ~0.04 μm. This is much less than the calculated depth of penetration of the thin film of 0.52 μm (70), so that the entire film should be interrogated by the infrared beam.

The O_3/O_2 mixture, generated by photolysis of O_2 (Praxair, 99.993%) using a low-pressure mercury lamp (UV Products, model D-23017), was diluted in a 5-L glass mixing bulb to obtain O_3 concentrations ranging from 130 ppb to 1,150 ppb. This mixture flowed through the ATR cell (*SI Appendix*, Fig. S5A), exposing the thin NPM film to a constant concentration of O_3 in each experiment, during which the ATR infrared spectra were recorded using 128 scans at 4-cm^{-1} resolution on a Mattson Galaxy 5020 FTIR.

Quantitative Modeling. A challenge with quantifying rate constants for gas–solid reactions is that both diffusion into the film and reaction take place simultaneously (62, 63). If they occur on similar time scales, assuming a well-mixed condensed phase is not valid. Thus, quantitative modeling that integrates the time-dependent physical and chemical processes must be used. In the present case, KM-SUB (62) was applied. This model includes reversible adsorption, surface reactions, and exchange between the surface and the bulk, in addition to bulk diffusion and reaction. Outputs from the model include the time and concentration dependence of NPM. Varying the input parameters to obtain best fits to the data provides insights into the role of diffusion into the film occurring simultaneously with chemical reaction. A detailed description of the model is found in *SI Appendix*.

Data availability. All relevant data have been included in the text and *SI Appendix*.

1. A. Elbert, M. Haas, B. Springer, W. Thielert, R. Nauen, Applied aspects of neonicotinoid uses in crop protection. *Pest Manag. Sci.* **64**, 1099–1105 (2008).
2. A. M. Cimino, A. L. Boyles, K. A. Thayer, M. J. Perry, Effects of neonicotinoid pesticide exposure on human health: A systematic review. *Environ. Health Perspect.* **125**, 155–162 (2017).
3. T. J. Wood, D. Goulson, The environmental risks of neonicotinoid pesticides: A review of the evidence post 2013. *Environ. Sci. Pollut. Res. Int.* **24**, 17285–17325 (2017).
4. J. M. Bonmatin et al., Environmental fate and exposure; neonicotinoids and fipronil. *Environ. Sci. Pollut. Res. Int.* **22**, 35–67 (2015).
5. C. Botías et al., Neonicotinoid residues in wildflowers, a potential route of chronic exposure for bees. *Environ. Sci. Technol.* **49**, 12731–12740 (2015).
6. C. Botías et al., Response to comment on "Neonicotinoid residues in wildflowers, a potential route of chronic exposure for bees". *Environ. Sci. Technol.* **50**, 1630–1631 (2016).
7. H. Thompson, P. Campbell, Comment on "Neonicotinoid residues in wildflowers, a potential route of chronic exposure for bees." *Environ. Sci. Technol.* **50**, 1628–1629 (2016).
8. N. Simon-Delso et al., Systemic insecticides (neonicotinoids and fipronil): Trends, uses, mode of action and metabolites. *Environ. Sci. Pollut. Res. Int.* **22**, 5–34 (2015).
9. C. Giorio et al., An update of the Worldwide Integrated Assessment (WIA) on systemic insecticides. Part 1: New molecules, metabolism, fate, and transport. *Environ. Sci. Pollut. Res. Int.*, 10.1007/s11356-017-0394-3 (2017).
10. D. Goulson, REVIEW: An overview of the environmental risks posed by neonicotinoid insecticides. *J. Appl. Ecol.* **50**, 977–987 (2013).
11. D. Goulson, E. Nicholls, C. Botías, E. L. Rotheray, Bee declines driven by combined stress from parasites, pesticides, and lack of flowers. *Science* **347**, 1255957 (2015).
12. M. B. van Lexmond, J.-M. Bonmatin, D. Goulson, D. A. Noome, Worldwide Integrated Assessment on systemic pesticides: Global collapse of the entomofauna: Exploring the role of systemic insecticides. *Environ. Sci. Pollut. Res. Int.* **22**, 1–4 (2015).
13. J. P. van der Sluijs et al., Conclusions of the Worldwide Integrated Assessment on the risks of neonicotinoids and fipronil to biodiversity and ecosystem functioning. *Environ. Sci. Pollut. Res. Int.* **22**, 148–154 (2015).
14. L. Pisa et al., An update of the Worldwide Integrated Assessment (WIA) on systemic insecticides. Part 2: Impacts on organisms and ecosystems. *Environ. Sci. Pollut. Res. Int.*, 10.1007/s11356-017-0341-3 (2017).
15. European Union, Document L:2018:132:TOC. *Off. J. Eur. Union L* **132**, 61 (2018).
16. Pest Management Regulatory Agency, "Proposed re-evaluation decision Report PRVD2018-12, imidacloprid and its associated end-use products: Pollinator re-evaluation" (Government of Canada, Ottawa, ONT, Canada, 2018).
17. B. J. Finlayson-Pitts, J. N. Pitts, Chemistry of the Upper and Lower Atmosphere: Theory, Experiments, and Applications (Academic, 2000).
18. K. Z. Aregahegn, D. Shemesh, R. B. Gerber, B. J. Finlayson-Pitts, Photochemistry of thin solid films of the neonicotinoid imidacloprid on surfaces. *Environ. Sci. Technol.* **51**, 2660–2668 (2017).
19. T. Ding, D. Jacobs, B. K. Lavine, Liquid chromatography-mass spectrometry identification of imidacloprid photolysis products. *Microchem.* **99**, 535–541 (2011).
20. T. Ding, B. K. Lavine, Separation of imidacloprid and its degradation products using reversed phase liquid chromatography with water rich mobile phases. *J. Chromatogr. A* **1218**, 9221–9226 (2011).
21. Z. Lu, J. K. Challis, C. S. Wong, Quantum yields for direct photolysis of neonicotinoid insecticides in water: Implications for exposure to nontarget aquatic organisms. *Environ. Sci. Technol. Lett.* **2**, 188–192 (2015).

22. D. Redlich, N. Shahin, P. Ekici, A. Friess, H. Parlar, Kinetical study of the photoinduced degradation of imidacloprid in aquatic media. *Clean (Weinh.)* **35**, 452–458 (2007).

23. N. Schippers, W. Schwack, Photochemistry of imidacloprid in model systems. *J. Agric. Food Chem.* **56**, 8023–8029 (2008).

24. N. Schippers, W. Schwack, Phototransformation of imidacloprid on isolated tomato fruit cuticles and on tomato fruits. *J. Photochem. Photobiol. B* **98**, 57–60 (2010).

25. S. L. Chao, J. E. Casida, Interaction of imidacloprid metabolites and analogs with the nicotinic acetylcholine receptor of mouse brain in relation to toxicity. *Pestic. Biochem. Physiol.* **58**, 77–88 (1997).

26. J. Pichtel, Distribution and fate of military explosives and propellants in soil: A review. *Appl. Environ. Soil Sci.* **2012**, 617236 (2012).

27. E. C. Koch, Insensitive high explosives: III. Nitroguanidine-synthesis-structure-spectroscopy-sensitiveness. *Propellants Explos. Pyrotech.* **44**, 267–292 (2019).

28. M. I. Walash, F. Belal, F. Ibrahim, M. Hefnawy, M. Eid, Kinetic spectrophotometric method for the determination of ranitidine and nizatidine in pharmaceuticals. *J. AOAC Int.* **85**, 1316–1323 (2002).

29. C. McCoy, A. B. Broce, M. W. Dryden, Flea blood feeding patterns in cats treated with oral nitenpyram and the topical insecticides imidacloprid, fipronil and selamectin. *Vet. Parasitol.* **156**, 293–301 (2008).

30. M. K. Rust, M. M. Waggoner, N. C. Hinkle, D. Stansfield, S. Barnett, Efficacy and longevity of nitenpyram against adult cat fleas (Siphonaptera: Pulicidae). *J. Med. Entomol.* **40**, 678–681 (2003).

31. R. Schenker, O. Tinembart, E. Humbert-Droz, T. Cavaliero, B. Yerly, Comparative speed of kill between nitenpyram, fipronil, imidacloprid, selamectin and cythioate against adult *Ctenocephalides felis* (Bouché) on cats and dogs. *Vet. Parasitol.* **112**, 249–254 (2003).

32. S. Ahmed, M. S. Nisar, M. M. Shakir, M. Imran, K. Iqbal, Comparative efficacy of some neonicotinoids and traditional insecticides on sucking insect pests and their natural enemies on BT-121 cotton crop. *J. Anim. Plant Sci.* **24**, 660–663 (2014).

33. S. Y. Wang *et al.*, Sublethal and transgenerational effects of short-term and chronic exposures to the neonicotinoid nitenpyram on the cotton aphid *Aphis gossypii*. *J. Pest. Sci.* **90**, 389–396 (2017).

34. Z. Q. Zhang *et al.*, Nitenpyram seed treatment effectively controls against the mirid bug *Apolygus lucorum* in cotton seedlings. *Sci. Rep.* **7**, 8572 (2017).

35. P. Zhang *et al.*, Efficacy of granular applications of clothianidin and nitenpyram against *Aphis gossypii* (Glover) and *Apolygus lucorum* (Meyer-Dur) in cotton fields in China. *Crop Prot.* **78**, 27–34 (2015).

36. K. Z. Aregahegn, M. J. Ezell, B. J. Finlayson-Pitts, Photochemistry of solid films of the neonicotinoid nitenpyram. *Environ. Sci. Technol.* **52**, 2760–2767 (2018).

37. S. A. Todey, A. M. Fallon, W. A. Arnold, Neonicotinoid insecticide hydrolysis and photolysis: Rates and residual toxicity. *Environ. Toxicol. Chem.* **37**, 2797–2809 (2018).

38. I. González-Mariño, I. Rodríguez, L. Rojo, R. Cela, Photodegradation of nitenpyram under UV and solar radiation: Kinetics, transformation products identification and toxicity prediction. *Sci. Total Environ.* **644**, 995–1005 (2018).

39. P. S. Bailey, *Ozonation in Organic Chemistry* (Academic, 1978), vol. I.

40. P. S. Bailey, *Ozonation in Organic Chemistry* (Academic, 1982), vol. II.

41. R. Criegee, Ozone. *Chemiker-Zeitung* **99**, 138–141 (1975).

42. M. A. H. Khan, C. J. Percival, R. L. Caravan, C. A. Taatjes, D. E. Shallcross, Criegee intermediates and their impacts on the troposphere. *Environ. Sci. Process. Impacts* **20**, 437–453 (2018).

43. C. A. Taatjes, D. E. Shallcross, C. J. Percival, Research frontiers in the chemistry of Criegee intermediates and tropospheric ozonolysis. *Phys. Chem. Chem. Phys.* **16**, 1704–1718 (2014).

44. M. I. Lester, S. J. Klippenstein, Unimolecular decay of Criegee intermediates to OH radical products: Prompt and thermal decay processes. *Acc. Chem. Res.* **51**, 978–985 (2018).

45. E. C. Tuazon, R. Atkinson, S. M. Aschmann, J. Arey, Kinetics and products of the gas-phase reactions of O_3 with amines and related compounds. *Res. Chem. Intermed.* **20**, 303–320 (1994).

46. M. J. Ezell *et al.*, Experimental and theoretical studies of the environmental sensitivity of the absorption spectra and photochemistry of nitenpyram and analogs. *ACS Earth Space Chem.* **3**, 2063–2075 (2019).

47. A. G. Cook, *Enamines. Synthesis, Structure and Reactions* (Marcel Dekker, 1988).

48. Z. Rappoport, *The Chemistry of Enamines* (Wiley, 1994), vol. 1.

49. D. Jeon *et al.*, Transformation of ranitidine during water chlorination and ozonation: Moiety-specific reaction kinetics and elimination efficiency of NDMA formation potential. *J. Hazard. Mater.* **318**, 802–809 (2016).

50. G. Socrates, *Infrared and Raman Characteristic Group Frequencies* (Wiley, ed. 3, 2004).

51. M. P. Strobel, L. Morin, D. Paquer, Action of ozone on vinyl derivatives-reactions retaining carbon chain. *Tetrahedron Lett.* **21**, 523–524 (1980).

52. B. Witkop, Imine-enamine systems and the mechanism of their oxidation. *J. Am. Chem. Soc.* **78**, 2873–2882 (1956).

53. G. Pitacco, E. Valentin, "Oxidation and reduction of enamines" in *The Chemistry of Enamines*, Z. Rappoport, Ed. (Wiley, 1994), vol. 2, pp. 923–992.

54. W. S. Barney *et al.*, Infrared absorption cross-section measurements for nitrous acid (HONO) at room temperature. *J. Phys. Chem. A* **104**, 1692–1699 (2000).

55. W. S. Barney *et al.*, Additions and corrections. *J. Phys. Chem. A* **105**, 4166 (2001).

56. B. J. Finlayson-Pitts, L. M. Wingen, A. L. Sumner, D. Syomin, K. A. Ramazan, The heterogeneous hydrolysis of NO_2 in laboratory systems and in outdoor and indoor atmospheres: An integrated mechanism. *Phys. Chem. Chem. Phys.* **5**, 223–242 (2003).

57. C. C. Lai, B. J. Finlayson-Pitts, W. V. Willis, Formation of secondary ozonides from the reaction of an unsaturated phosphatidylcholine with ozone. *Chem. Res. Toxicol.* **3**, 517–523 (1990).

58. T. M. McIntire, O. Ryder, B. J. Finlayson-Pitts, Secondary ozonide formation from the ozone oxidation of unsaturated self-assembled monolayers on ZnSe ATR crystals. *J. Phys. Chem. C* **113**, 11060–11065 (2009).

59. H. C. Allen, J. M. Laux, R. Vogt, B. J. Finlayson-Pitts, J. C. Hemminger, Water-induced reorganization of ultrathin nitrate films on NaCl: Implications for the tropospheric chemistry of sea salt particles. *J. Phys. Chem.* **100**, 6371–6375 (1996).

60. J. M. Laux, J. C. Hemminger, B. J. Finlayson-Pitts, X-ray photoelectron spectroscopic studies of the heterogenous reaction of gaseous nitric acid with sodium chloride: Kinetics and contribution to the chemistry of the marine troposphere. *Geophys. Res. Lett.* **21**, 1623–1626 (1994).

61. S. Zhou *et al.*, Multiphase reactivity of polycyclic aromatic hydrocarbons is driven by phase separation and diffusion limitations. *Proc. Natl. Acad. Sci. U.S.A.* **116**, 11658–11663 (2019).

62. M. Shiraiwa, C. Pfrang, U. Poschl, Kinetic multi-layer model of aerosol surface and bulk chemistry (KM-SUB): The influence of interfacial transport and bulk diffusion on the oxidation of oleic acid by ozone. *Atmos. Chem. Phys.* **10**, 3673–3691 (2010).

63. M. Shiraiwa, M. Ammann, T. Koop, U. Pöschl, Gas uptake and chemical aging of semisolid organic aerosol particles. *Proc. Natl. Acad. Sci. U.S.A.* **108**, 11003–11008 (2011).

64. L. Vereecken, A. Novelli, D. Taborrelli, Unimolecular decay strongly limits the atmospheric impact of Criegee intermediates. *Phys. Chem. Chem. Phys.* **19**, 31599–31612 (2017).

65. B. J. Finlayson-Pitts, Introductory lecture: Atmospheric chemistry in the anthropocene. *Faraday Discuss.* **200**, 11–58 (2017).

66. S. Gligorovski, Nitrous acid (HONO): An emerging indoor pollutant. *J. Photochem. Photobiol. Chem.* **314**, 1–5 (2016).

67. J. Kleffmann, Daytime sources of nitrous acid (HONO) in the atmospheric boundary layer. *ChemPhysChem* **8**, 1137–1144 (2007).

68. R. B. Cody, J. A. Laramée, H. D. Durst, Versatile new ion source for the analysis of materials in open air under ambient conditions. *Anal. Chem.* **77**, 2297–2302 (2005).

69. J. H. Gross, Direct analysis in real time–A critical review on DART-MS. *Anal. Bioanal. Chem.* **406**, 63–80 (2014).

70. N. J. Harrick, *Internal Reflection Spectroscopy* (Interscience, 1967).

71. L. Z. Xu, Z. Yang, X. Yi, G. W. An, (E)-N-(6-Chloro-3-pyridylmeth-yl)-N-ethyl-N'-methyl-2-nitro-ethyl-ene-1,1-diamine. *Acta Crystallogr. Sect. E Struct. Rep. Online* **64**, o1074 (2008).

ENVIRONMENTAL SCIENCES